



**HAL**  
open science

## Motion Corrected 3D Liver undersampled MRI

Felipe Yanez, Pablo Irarrazaval

► **To cite this version:**

Felipe Yanez, Pablo Irarrazaval. Motion Corrected 3D Liver undersampled MRI. 2014. hal-01080892v1

**HAL Id: hal-01080892**

**<https://inria.hal.science/hal-01080892v1>**

Preprint submitted on 6 Nov 2014 (v1), last revised 1 Jun 2015 (v2)

**HAL** is a multi-disciplinary open access archive for the deposit and dissemination of scientific research documents, whether they are published or not. The documents may come from teaching and research institutions in France or abroad, or from public or private research centers.

L'archive ouverte pluridisciplinaire **HAL**, est destinée au dépôt et à la diffusion de documents scientifiques de niveau recherche, publiés ou non, émanant des établissements d'enseignement et de recherche français ou étrangers, des laboratoires publics ou privés.

# Motion Corrected 3D Liver undersampled MRI

Felipe Yanez and Pablo Irarrazaval

*Department of Electrical Engineering, Pontificia Universidad Católica de Chile, Santiago, Chile.  
Biomedical Imaging Center, Pontificia Universidad Católica de Chile, Santiago, Chile.*

November 6, 2014

## Abstract

The emergence of sparse reconstruction methods for undersampled data in Magnetic Resonance Imaging (MRI), such as Compressed Sensing (CS), have been valuable tools to accelerate data acquisition while preserving accurate image reconstruction. However, sparse reconstruction methods, including CS, are not easy to apply when there is intra-frame motion. Such is the case of free-breathing dynamic MRI in the liver. It is difficult to avoid non-rigid motion artifacts, even more so in volumetric acquisitions. To avoid these kind of artifacts, we propose a new reconstruction technique tailored for dynamic liver imaging by estimating the motion between frames to correct inconsistencies in k-space measurements. In this work, we describe how the proposed method addresses an increase in image efficiency for free-breathing dynamic 3D liver MRI. Our approach produced results that demonstrate it is feasible to achieve a 10x speedup in acquisition time and remove motion artifacts without diminishing image quality. The proposed method produced gains up to 6 dB with respect of traditional CS framework.

**keywords:** compressed sensing; undersampling; sparse reconstruction; motion correction; non-rigid registration; liver.

## 1 Introduction

Image efficiency in Magnetic Resonance Imaging (MRI), i.e. the trade-off between acquisition time and image quality, has been widely studied in the MRI community. In the past, image efficiency improvements were shown to be directly related to hardware development, e.g. acquiring multiple lines in the readout after a single excitation to speed up data collection (Wright, 1997). Nowadays, we are at the point where physical and physiological restrictions are the main reasons for limiting the scanning speed (Lustig et al., 2007). In this sense, the emergence of new approaches handling the imaging problem with less data as required by the Nyquist-Shannon rate seem to provide an answer for further improvements in image efficiency.

These new approaches, also known as sparse reconstruction methods, rely on the idea of compressibility, which assumes redundancy in an image (Candes et al., 2006a,b). One

sparse reconstruction method for undersampled data of high impact in MRI is Compressed Sensing (CS) (Candes et al., 2006a,b; Candes and Tao, 2006; Donoho, 2006). CS is a relatively new concept in signal processing used to speed up MRI scanning time (Lustig et al., 2007). CS enables reliable image recovery for severely undersampled random measurements, if the desired signal is compressible in a known domain and the aliasing artifacts due undersampling are incoherent in the measurement domain (Candes et al., 2006a,b; Candes and Tao, 2006; Donoho, 2006). The CS framework has been used in different MRI applications, e.g. brain (Lustig et al., 2008), diffusion spectrum (Bilgic et al., 2012), quantitative susceptibility mapping (Yanez et al., 2013; Yanez and Irarrazaval, 2014), and multi-contrast reconstruction (Bilgic et al., 2011).

CS has been also applied in dynamic MRI, where most reconstruction methods use temporal correlations of the signal. A common approach is to exploit the sparsity of the residual signal after subtracting an initial estimate (Jung et al., 2009; Jung and Ye, 2010). In this way, the signal has a sparse representation, and it is possible to achieve more accurate results. A similar problem has been also studied in the field of video compression, where video images are compressed using the similarities between different frames to achieve high efficiency. Some ideas from video compression algorithms have been used in dynamic MRI reconstructions (Jung and Ye, 2010).

In MRI applications, dealing with motion is also an important issue for reconstruction methods because patient’s unwanted or involuntary motion during acquisition may lead to artifacts in the reconstructed images (Lustig et al., 2008; Usman et al., 2012). The presence of motion may also reduce the sparsity of the images (Usman et al., 2012). In this sense, a generalized motion correction framework was developed to correct non-rigid motion in the reconstructed images (Batchelor et al., 2005). This framework models motion-corrupted images through the application of a matrix equation. As demonstrated in (Batchelor et al., 2005; Prieto et al., 2007), it is possible to reconstruct a motion-corrected image using numerical matrix inversion algorithms.

In liver MRI, it is critical to have high spatial and temporal resolution to identify small structures or to evaluate the liver parenchyma perfusion to detect focal or diffuse perfusion defects. Additionally actual volumetric technique results in poor-resolution images due to they are obtained in patients with breath-hold limitations (Chandarana et al., 2012). Small structures such as tumor nodules up to 20 mm and tumor angiogenesis are hard to identify in low-quality images (Chandarana et al., 2011). Increasing spatial and temporal resolution can help to detect tumors in early stages, thereby avoiding surgery and instead treating the patient with curative therapy, which provides the best possible long-term survival at a lower cost (Lee et al., 2011; Naugler and Sonnenberg, 2010).

Herein, we propose a compressed sensing framework tailored for free-breathing 3D liver MRI with high spatial and temporal resolution. The proposed dynamic framework incorporates a generalized non-rigid motion registration between frames (Myronenko, 2010; Hill et al., 2001) to correct inconsistencies in k-space and increase the number of samples to recover a motion corrected image under a CS reconstruction method (Usman et al., 2012). At each frame, the number of measurements is severely below the Nyquist-Shannon rate. Parallel imaging was used in this work, applying the proposed method independently to each coil. We performed this approach in 3D in-vivo experiments using various undersampling factors, obtaining improved signal-to-error ratios with respect to traditional CS technique

and accurate complex wavelet structural similarity indexes with the ground truth.

## 2 Theory

In this section we first present the imaging problem to solve, followed by the proposed reconstruction technique.

### 2.1 Imaging

In traditional dynamic MRI, the acquisition is done at the same respiratory position to avoid motion artifacts (Figure 1 (a)). Instead, we will consider sampling at different breathing positions, i.e. the acquired data in a respiratory cycle of  $T$  possible motion states (frames) delivers a collection of  $T$  images, as illustrated in Figure 1 (b). We assume that at a particular discrete time  $t \in \{1, \dots, T\}$ , all acquired k-space values are consistent, i.e. each frame is free of motion artifacts.

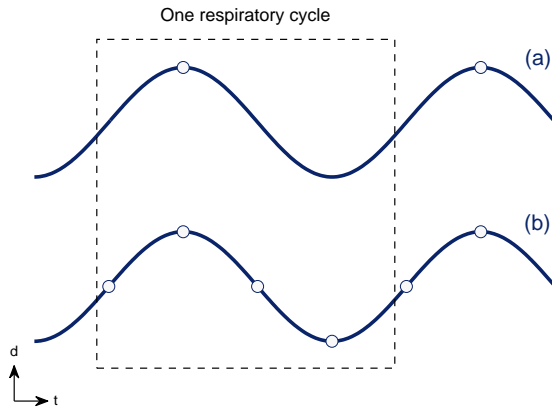


Figure 1: Representation of two acquisition approaches employed in dynamic MRI, considering measurements at different translational displacement positions across time. (a) Traditional acquisition technique, the acquired data in a respiratory cycle of  $T$  possible frames delivers a collection of few images ( $\ll T$ ). (b) Proposed acquisition technique, the acquired data in a respiratory cycle of  $T$  possible frames delivers a collection of  $T$  severely undersampled images.

Let us define  $\mathbf{m}_t \in \mathbb{C}^N$  as the underlying vector form of the three-dimensional complex-valued true MR images in the canonical domain at discrete times  $t \in \{1, \dots, T\}$ ,  $\mathbf{b}_t \in \mathbb{C}^P$  as the vector form of the k-space undersampled noisy measurements of  $\mathbf{m}_t$  (considering  $P \ll N$ ), and  $\mathbf{e}_t \in \mathbb{C}^P$  as the corresponding acquisition noise. To facilitate notation, we will drop the subindex  $t$ , and will assume that it represents the vector form at all discrete times  $t \in \{1, \dots, T\}$ . With this, the imaging procedure can be written as

$$\mathbf{b} = \mathbf{S}\mathbf{F}\mathbf{m} + \mathbf{e}, \quad (1)$$

where  $\mathbf{F}$  is the 3D Fourier transform operator that transforms independently each frame to k-space, and  $\mathbf{S}$  is the sampling operator that randomly undersamples the k-space data from each frame.

We can also describe  $\mathbf{m}$  from a reference frame  $\mathbf{m}_{t_0} \in \mathbb{C}^N$  by using the motion information between each frame and the reference (Prieto et al., 2007). We denote  $\mathbf{V}$  as a motion operator that warps the pixels from an arbitrary reference image  $\mathbf{m}_{t_0}$  to the positions at all possible times. In operator form, this is

$$\mathbf{m} = \mathbf{V}\mathbf{m}_{t_0}, \quad (2)$$

such that Equation (1) becomes

$$\mathbf{b} = \mathbf{S}\mathbf{F}\mathbf{V}\mathbf{m}_{t_0} + \mathbf{e}. \quad (3)$$

As k-space has been severely undersampled ( $P \ll N$ ), the system in Equation (3) is ill-posed, i.e. it does not satisfy the Nyquist-Shannon sampling rate. To measure the degree of undersampling, we define the acceleration factor as  $R = N/P$ . For image recovery, we need additional information, i.e. we need to formulate a regularized version of Equation (3), where, the structure of the true images is key.

## 2.2 Reconstruction

We propose to address the reconstruction of a motion corrected image by solving an optimization problem for a reference image  $\mathbf{m}_{t_0} \in \mathbb{C}^N$ , chosen from any of the  $T$  possible frames in the respiratory cycle.

A comprehensive theory to tackle this problem was proposed by Tikhonov and Arsenin (1977), where information of the underlying signals was incorporated to the model. This information is the so-called regularization or penalization

$$\hat{\mathbf{m}}_{t_0} = \arg \min_{\mathbf{m}_{t_0}} \frac{1}{2} \|\mathbf{S}\mathbf{F}\mathbf{V}\mathbf{m}_{t_0} - \mathbf{b}\|_{\ell_2}^2 + \tau \frac{1}{2} \|\Psi\mathbf{m}_{t_0}\|_{\ell_2}^2, \quad (4)$$

where  $\|\mathbf{u}\|_{\ell_p} = (\sum_{i=1}^n |u_i|^p)^{1/p}$  is the  $p$ -norm of vector  $\mathbf{u} \in \mathbb{R}^n$ , letting  $p \geq 1$  be a real number,  $\tau$  is the regularization parameter that weights the trade-off between the data consistency ( $\frac{1}{2} \|\mathbf{S}\mathbf{F}\mathbf{V}\mathbf{m}_{t_0} - \mathbf{b}\|_{\ell_2}^2$ ) and the penalization ( $\frac{1}{2} \|\Psi\mathbf{m}_{t_0}\|_{\ell_2}^2$ ),  $\Psi$  is an operator that ensures smoothness in the underlying image, and the motion operator  $\mathbf{V}$  is known. The solution of this problem is also known and has a closed form. The main problem with the  $\ell_2$ -regularization method is that the smoothness assumption is not always true in medical imaging.

The CS approach was introduced in 2006 by Candes et al. (2006a,b); Candes and Tao (2006) and Donoho (2006). In medical imaging,  $\ell_1$ -regularization fits very well since they can be represented in a sparse domain. Comparing to Tikhonov and Arsenin's regularization, sparse reconstruction methods also have the advantage of achieving more accurate results with high acceleration factors (Ng, 2004). The  $\ell_1$ -regularization method does not have a closed form solution, but it can be solved using efficient first-order optimization methods (Lustig et al., 2007; Becker et al., 2011; Boyd and Vandenberghe, 2004).

We propose a second-order cone program that minimizes the regularized version of Equation (3), i.e. the  $\ell_1$  norm of a sparse representation of  $\mathbf{m}_{t_0}$ , with the data consistency constraints (Candes and Tao, 2005)

$$\begin{aligned}
& \underset{\mathbf{m}_{t_0}}{\text{minimize}} && \|\Phi \mathbf{m}_{t_0}\|_{\ell_1} \\
& \text{subject to} && \frac{1}{2} \|\mathbf{S}\mathbf{F}\mathbf{V}\mathbf{m}_{t_0} - \mathbf{b}\|_{\ell_2}^2 < \sigma,
\end{aligned} \tag{5}$$

where  $\Phi$  is a sparsifying operator, e.g. wavelet, or total variation, and  $\sigma$  is a small positive number that controls data fidelity, usually determined by the noise level.

Prior to solving the minimization problem (5), we need to find an approximation to the motion operator  $\mathbf{V}$ . This can be done as follows:

- Compute an initial reconstruction using a CS framework for each frame.
- Define a reference frame and estimate the motion vectors by registering all frames to the reference (Irrazaval et al., 2005).
- Finally, define  $\mathbf{V}$  using this registration to align frames to the reference, and the inverse registration function is used to warp the reference to all possible frames.

### 2.2.1 Initial reconstruction

For a preliminary estimation, we exploit temporal correlations assuming sparsity of the residual signal after subtraction of an initial estimate of the mean (Jung et al., 2009). We first compute the mean of the measurements, denoted as  $\bar{\mathbf{b}}$ .

Now, the zero-mean measurements are computed as

$$\mathbf{b}'_t = \mathbf{b}_t - \bar{\mathbf{b}}, \quad \forall t \in \{1, \dots, T\}. \tag{6}$$

A zero-mean CS recovery is applied independently to the residual of each frame  $\mathbf{b}'_t$ . Because of the sparsity of the residual image, we select the canonical domain as the sparse domain. The zero-mean CS reconstruction is defined as follows:

$$\hat{\mathbf{m}}' = \arg \min_{\mathbf{m}'} \frac{1}{2} \|\mathbf{S}\mathbf{F}\mathbf{m}' - \mathbf{b}'\|_{\ell_2}^2 + \beta \|\mathbf{m}'\|_{\ell_1}, \tag{7}$$

where  $\beta$  is the regularization parameter. The initial reconstruction is computed by adding the mean image in the canonical domain to each residual estimation,

$$\hat{\mathbf{m}}_t = \hat{\mathbf{m}}'_t + \mathbf{F}^H \bar{\mathbf{b}}, \quad \forall t \in \{1, \dots, T\}, \tag{8}$$

where  $\mathbf{F}^H$  is the Hermitian transpose of  $\mathbf{F}$ .

### 2.2.2 Motion vectors estimation

The reconstructed frames allow us to select a reference image. The reference frame is usually chosen at end expiration when the liver is moving less. Each preliminary estimation is registered to the reference frame using a fast and efficient adaptive regularization approach for non-rigid image registration (Myronenko, 2010).

Our registration method relies on a Bayesian formulation, where we estimate the prior distribution on parameters assuming that it is close to some given model distribution. We constrain the prior distribution to be a Gauss-Markov random field, which allows us to solve

for the prior distribution analytically and provides a fast optimization algorithm (Myronenko, 2010),

$$\mathbf{V}_t = \arg \min_{\mathbf{v}_t} \frac{1}{w} D(\hat{\mathbf{m}}_t, \hat{\mathbf{m}}_{t_0} | \mathbf{v}_t) + \|\mathbf{k}^T \mathbf{Q} \mathbf{v}_t\|_{\ell_1}, \quad \forall t \in \{1, \dots, T\}, \quad (9)$$

where  $D(\hat{\mathbf{m}}_t, \hat{\mathbf{m}}_{t_0} | \mathbf{v}_t)$  is a similarity measure, e.g. Mutual Information (MI) (Viola and Wells, 1997), Sum of Squared Differences (SSD), or Sum of Absolute Differences (SAD),  $w$  is the weight between data consistency and penalization,  $\mathbf{k}$  are the squared-root-eigenvalues of the model distribution,  $\mathbf{Q}$  is a matrix containing the eigenvectors of the inverse covariance shift-invariant matrix. In a prior distribution constrained to be a Gauss-Markov random field, the eigenvalues and eigenvectors have a known form (Myronenko, 2010). Motion operator  $\mathbf{V}$  is defined by the motion vectors  $\mathbf{V}_t$  obtained from the proposed registration algorithm. The motion vectors are obtained pixel-wise for every frame.

### 2.2.3 MC-CS recovery

To recover the motion corrected image,  $\hat{\mathbf{m}}_{t_0}$ , the acquired data from all the motion states (frames)  $\mathbf{b}$  and the estimated motion vectors operator  $\mathbf{V}$  are needed as shown in Equation (5). Considering the noise level in the  $\lambda$  regularization parameter, the unconstrained version of the minimization problem in Equation (5) is the following convex problem

$$\hat{\mathbf{m}}_{t_0} = \arg \min_{\mathbf{m}_{t_0}} \frac{1}{2} \|\mathbf{S} \mathbf{F} \mathbf{V} \mathbf{m}_{t_0} - \mathbf{b}\|_{\ell_2}^2 + \lambda \|\Phi \mathbf{m}_{t_0}\|_{\ell_1}. \quad (10)$$

## 3 Methods

The goal of the proposed technique is to reconstruct a motion corrected 3D liver image from undersampled pseudorandom measurements. The main contribution is employing motion-corrected inconsistent k-space samples from different frames into a CS reconstruction framework to estimate a single higher quality image. To correct motion, we estimate the motion vectors between different frames. To compute the motion vectors we perform a preliminary CS reconstruction to each frame, and subsequently, we register those reconstructed images to a reference frame. The obtained motion vectors generate the motion operator  $\mathbf{V}$ , which is an invertible matrix (Batchelor et al., 2005). Figure 2 shows a block diagram with the proposed algorithm steps.

In order to have the ground truth, we simulated a free-breathing acquisition, we performed a conventional 3D T1-weighted fast field echo sequence with fully sampled cartesian trajectory in the liver of healthy volunteers to generate the in-vivo dataset. We asked the volunteers to hold their breaths at different inspiration levels. Previously, a low-resolution image was acquired as a prescan. Informed consent was obtained from volunteers prior to imaging. A four-element body coil was used for all acquisitions using a Philips Achieva 1.5 T scanner (Philips Healthcare, Best, The Netherlands).

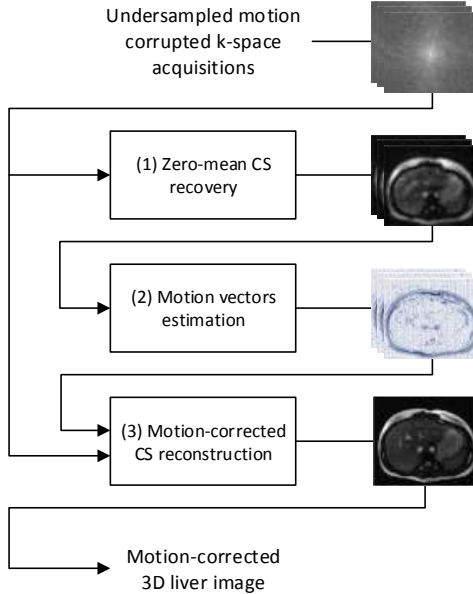


Figure 2: Block diagram of the proposed free-breathing dynamic 3D liver MRI reconstruction framework. (1) From the acquired undersampled motion corrupted samples, the mean of the data is subtracted. A CS recovery is performed to the residual, independently for each of the  $T$  frames. The estimation of each image is computed as the sum of the corresponding CS recovery with the mean image in the canonical domain. (2) The reconstructed images allows us to select a reference frame, usually chosen at end expiration where the liver is moving less. The  $T$  reconstructed frames are registered to the reference image, to compute the corresponding motion vectors. (3) The undersampled motion corrupted k-space acquisitions and the previously computed motion vectors are used to perform a motion corrected CS reconstruction to obtain a high resolution 3D liver image.

### 3.1 Reconstruction protocol

To solve Equations (10) and (7), two different  $\ell_1$ -norm penalized non-linear conjugate gradients with fast & cheap backtracking line-search reconstruction were implemented in Matlab (R2011a, The MathWorks, Inc., Natick, MA) (Lustig et al., 2007). A pseudo-code of both algorithms can be found in the Appendix.

To run the algorithms, we used a standard personal computer. In both reconstructions, we performed a maximum of 150 conjugate gradient iterations. Equation (10), for computational efficiency, was solved using the Hermitian-symmetric form for data consistency:

$$\mathbf{V}^H \mathbf{F}^H \mathbf{S}^H \mathbf{S} \mathbf{F} \mathbf{V}_{m_{t_0}} = \mathbf{V}^H \mathbf{F}^H \mathbf{S}^H \mathbf{b}.$$

For Equations (10) and (7), we selected optimal  $\lambda$  and  $\beta$  via the computation of the L-curve criterion (Hansen, 2000). In this case, optimal regularization parameters lie on the corner of the L-curve (Hansen, 1992), but sometimes it is difficult to distinguish it. In these cases we used the criteria proposed by Hansen and O’Leary of choosing the point with maximum curvature to be the optimal point (Hansen and O’Leary, 1993).

In Equation (10), the sparse representation is obtained via wavelet transformation, where the wavelet transform operator  $\Phi$  is an especially effective and computationally efficient biorthogonal wavelet: Cohen-Daubechies-Feauveau 9/7 (CDF 9/7) wavelet transform (Mat-

lab code available online at <http://www.getreuer.info/home/waveletcdf97>), which was reported to yield high quality sparse approximations for simulated diffusion propagators (Merlet et al., 2012). In Equation (7), the sparse representation is in the canonical domain.

### 3.2 In-vivo experiments

We simulated a free-breathing acquisition by performing a conventional breath-held 3D T1-weighted fast field echo sequence with fully sampled cartesian trajectory in the liver of four healthy volunteers to generate the in-vivo dataset. We asked the volunteers to hold their breaths at five different inspiration levels. For liver imaging, a four-element body coil was used, and the measurements were obtained with the following parameters: TR = 4.1 ms, TE = 1.95 ms, FOV =  $160 \times 224 \times 150$  mm<sup>3</sup>, flip angle = 10°, slice thickness = 10 mm, dynamic scans = 8, spatial resolution = 2 mm isotropic, dynamic scan time = 14.8 s.

The coil sensitivity maps were estimated by preliminarily acquiring a fully-sampled low-resolution image prior to the 3D T1-weighted fast field echo sequence. Both acquisitions had identical previously defined scan parameters. A smoothing filter was applied to the low-resolution images from each coil. The estimated maps were found to be the normalization of each smoothed low-resolution image by computing the sum-of-squares of all coil images.

Undersampled k-space data were obtained with different sampling pattern for each frame, which were generated using a Monte Carlo algorithm with minimum peak interference according to a particular acceleration factor ( $R$ ) (Lustig et al., 2007). The random sampling pattern is based on a polynomial variable density function, i.e. the low-frequency regions are more dense than the higher frequency regions. The number of samples from each frame is determined by the probability density function and the sampling factor ( $R$ ). We also enabled a sampling pattern that does not require a probability density function (results not shown). In-vivo experiments were performed at various sampling factors ( $R$ ).

To compute  $\mathbf{V}$ , the CS reconstructions from each receiver coil were combined using the sum of squares prior to registration. The reference image (frame) is chosen from previous combined reconstructions. We set as the reference the most common respiratory motion state at end expiration when the liver is moving less. All CS estimations are non-rigidly registered to the reference using an adaptive image registration algorithm (Myronenko, 2010). We used this registration to align frames to the reference, and the inverse registration function to warp the reference to all possible frames. Motion operator  $\mathbf{V}$  is constructed with these two functions.

We performed the registration algorithm that solves Equation (9) using the Mutual Information (MI) (Viola and Wells, 1997) similarity measure. We considered 250 iterations of a single hierarchical level with a mesh window size of 16 voxels.

We used the motion operator  $\mathbf{V}$  and undersampled k-space data to reconstruct the underlying motion corrected 3D liver image using the proposed technique. To test accuracy in reconstructions, we considered the signal-to-error ratio (SER)

$$SER = 20 \log_{10} \left( \frac{\|\mathbf{y}\|_{\ell_2}}{\|\mathbf{x} - \mathbf{y}\|_{\ell_2}} \right), \quad (11)$$

and the complex wavelet structural similarity (CW-SSIM) index (Sampat et al., 2009) defined as

$$CW-SSIM = \frac{2|\sum_{i=1}^n c_{x,i}c_{y,i}^*| + K}{\sum_{i=1}^n |c_{x,i}|^2 + \sum_{i=1}^n |c_{y,i}|^2 + K}, \quad (12)$$

where in both cases  $\mathbf{x} \in \mathbb{R}^m$  and  $\mathbf{y} \in \mathbb{R}^m$  are the absolute value vector representation of the estimated image and the true image, respectively. In the CW-SSIM index,  $\mathbf{c}_x \in \mathbb{C}^n$  and  $\mathbf{c}_y \in \mathbb{C}^n$  represent the wavelet coefficients of images  $\mathbf{x}$  and  $\mathbf{y}$ ;  $()^*$  represents the complex conjugation operation; and  $K$  represents a small positive constant to achieve accurate performance in local low contrast regions (Sampat et al., 2009). SER and CW-SSIM are measures quantified in dB and %, respectively.

## 4 Results

The proposed technique was tested on the in-vivo dataset with breath-held 3D liver MRI data simulating five different motion states. The performance of the proposed Motion-Corrected Compressed Sensing technique (MCCS) was compared against a traditional CS reconstruction (CS).

### 4.1 Regularization parameters

We selected optimal settings for the MCCS and CS frameworks. Computations of the L-curve were performed on the in-vivo dataset using several reduction factors ( $R$ ), and selecting the operating point with maximum curvature.

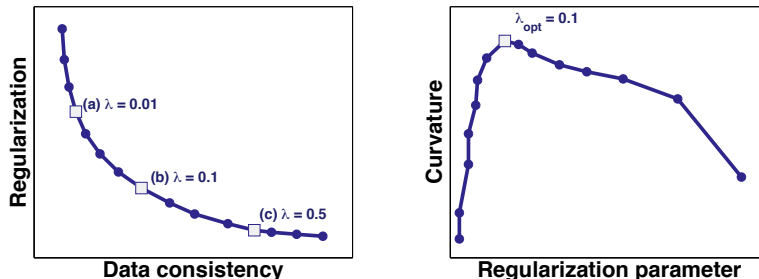


Figure 3: Optimal parameter selection for the traditional CS method. The L-curve was computed on the left, where the X-axis represents the data consistency term  $\frac{1}{2}\|\mathbf{S}\mathbf{F}\mathbf{V}\mathbf{m}_{t_0} - \mathbf{b}\|_{\ell_2}^2$ , and the Y-axis represents the regularization term  $\|\Phi\mathbf{m}_{t_0}\|_{\ell_1}$ . We solved Equation (10) for 15 values of fixed  $\lambda$ . On the right, we illustrate the computation of the curvature as function of the regularization parameter.

Figures 3 and 4 illustrate the L-curve and curvature of the regularization parameters for Equations (10) and (7) with 5-fold acceleration. For both cases, setting  $\lambda = 0.01$  and  $\beta = 0.002$ , defined in Figures 3 (a) and 4 (a), yielded to an under-regularized image reconstruction, whereas using  $\lambda = 0.5$  and  $\beta = 0.2$ , as in Figures 3 (c) and 4 (c), resulted in an over-regularized image reconstruction. For both cases, the second column in Figures 3 and 4 illustrates the computation of the curvature as function of the regularization parameter, where  $\lambda$  and  $\beta$  as defined in Figures 3 (b) and 4 (b) were the operating point that maximized the curvature. Therefore,  $\lambda_{opt} = 0.1$  and  $\beta_{opt} = 0.04$  were the optimal regularization parameters. All MCCS and CS reconstructions are performed with these optimal settings.

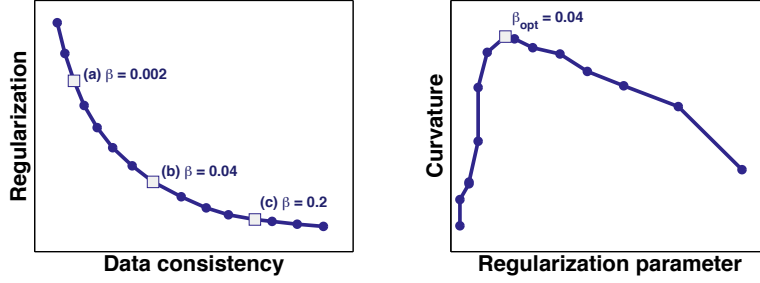


Figure 4: Optimal parameter selection for the traditional CS method. The L-curve was computed on the left, where the X-axis represents the data consistency term  $\frac{1}{2} \|\mathbf{S}\mathbf{F}\mathbf{m}' - \mathbf{b}'\|_{\ell_2}^2$ , and the Y-axis represents the regularization term  $\|\mathbf{m}'\|_{\ell_1}$ . We solved Equation (7) for 15 values of fixed  $\beta$ . On the right, we illustrate the computation of the curvature as function of the regularization parameter.

## 4.2 Image recovery

The proposed technique was tested on the in-vivo dataset with breath-held 3D liver MRI data simulating a free-breathing acquisition. This could represent a realistic case if we consider

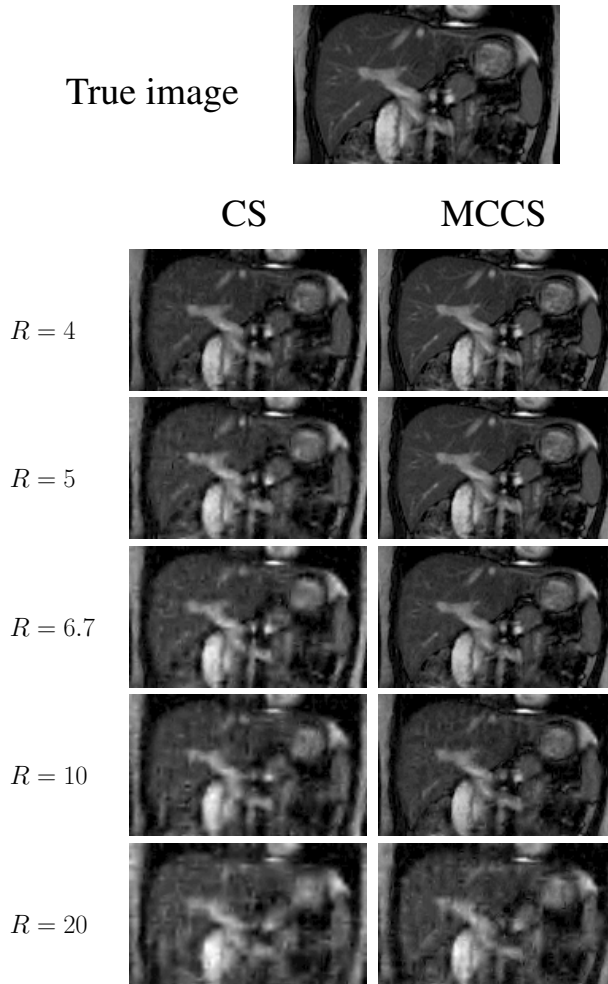


Figure 5: Results obtained using the MCCS and CS methods at different  $R$ .

that with a 5x undersampling, where the total scan time per frame would be 3 s during which we assume that the liver does not move significantly. This means a scan time per frame in the range of 1 to 4 s, depending on the undersampling rate.

The ground truth, fully-sampled image is illustrated in Figure 5 displaying a coronal slice. The first out of eight frames was set as the reference. The performance of the proposed MCCS technique, tailored for free-breathing acquisitions, was compared against a traditional CS reconstruction of the reference frame. In our experiments, we downsampled the data according to different sampling patterns ( $\mathbf{S}$ ) using acceleration factors from  $R = 4$  to  $R = 20$ . Figure 5 presents the traditional CS and proposed MCCS reconstructions at reduction factors of 4, 5, 6.7, 10 and 20. For the CS reconstructions, motion artifacts due to severely undersampling k-space became more evident as  $R$  increases. Preservation of sharp edges and correction of motion artifacts can be observed in the MCCS reconstructions.

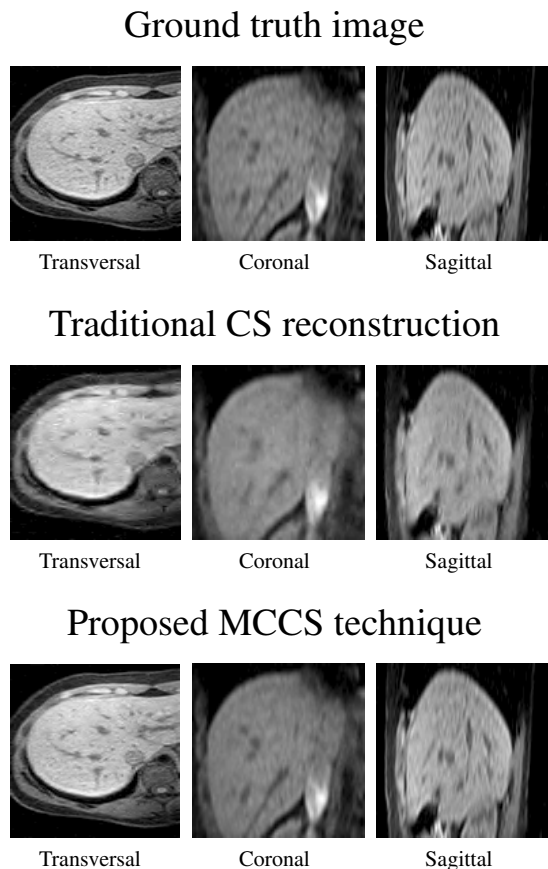


Figure 6: Reconstructed body planes using the MCCS and CS methods at different  $R$ .

We display the three orthogonal body planes reconstructions at  $R = 6.7$  for the ground truth image, the traditional CS reconstruction and the proposed MCCS technique (Figure 6). It can be appreciated that the proposed method recovered an accurate image, whereas artifacts remained for the CS reconstruction because of the few measurements.

### 4.3 Computation of ratios

The proposed MCCA reconstruction method with optimal settings at different acceleration factors was compared against a traditional CS framework. Figure 7 illustrates the signal-to-error ratio as function of  $R$ . Reconstructions obtained with the proposed technique reported more accurate results, with SER gains up to 6 dB compared to the traditional CS framework.

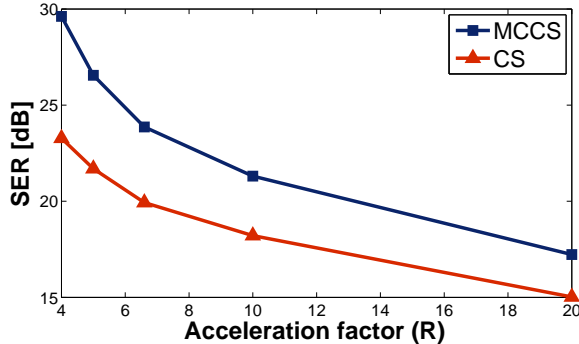


Figure 7: Computation of the reconstruction SER for the proposed motion-corrected CS recovery (MCCA) and traditional CS framework (CS) at different acceleration factors ( $R$ ) using the 3D-liver in-vivo dataset.

Four different volunteers were scanned to create the underlying dataset. To test the robustness of the proposed technique, the CW-SSIM index between the ground truth and each MCCA reconstruction was computed for several reduction factors. Figure 8 illustrates a plot of the mean and standard deviation of the index as a function of  $R$ . Reported results show that the proposed technique is stable under high reduction factors (approximately up to  $R = 10$ ). At higher reduction factors, the motion information estimation is poor, leading to unstable MCCA reconstructions.

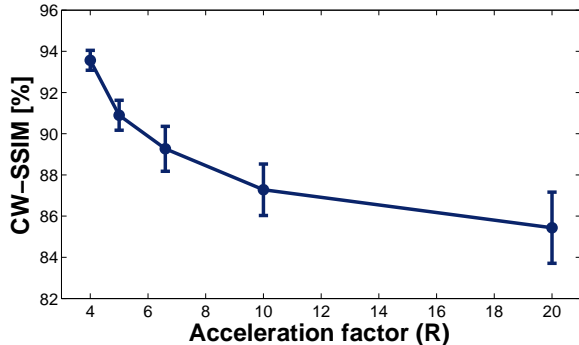


Figure 8: Computation of the reconstruction CW-SSIM index using the MCCA technique for the 4 volunteers of the dataset at different acceleration factors ( $R$ ). The mean CW-SSIM index of the 4 MCCA reconstructions is illustrated as a function of  $R$ , with its respective standard deviation.

## 5 Discussion

We proposed a motion corrected reconstruction technique tailored for dynamic 3D liver undersampled MRI. The main contribution is to employ motion-corrected inconsistent k-space

samples from different motion states (frames) of the liver into a CS reconstruction framework to estimate a motion corrected image (Usman et al., 2012). As shown in the results, this technique achieved accurate and reliable reconstructions in the in-vivo experiments (Figures 5, 6, 7 and 8). Although we are not testing our method with truly free-breathing data, we are confident that the results hold because for most of the respiratory cycle the quasi-static assumption for the liver is valid, and therefore we will have intra-frame k-space consistency most of the time.

To correct motion, we estimated the motion vectors between different motion states (frames) by using CS to reconstruct each frame and by registering these images to a reference. The CS framework recovers structured images by relying on compressibility, i.e. high contrast components are chosen over low contrast (Figures 5 and 6). In addition, registration also favors high contrast samples, which leads to decreased signal-to-error ratios outside the liver (higher contrast region) (Usman et al., 2012; Asif et al., 2012). We have used an adaptive non-rigid registration algorithm (Myronenko, 2010) to estimate the inter-frame motion between different frames. A source of improvement to the current theory may be to estimate motion vectors within neighboring frames in the form of a linear dynamical system instead of estimating them with respect to a single reference motion state (Asif et al., 2012).

The main limitations of this work can be grouped as follows: architecture and implementation. As shown in Figure 2, the architecture of the proposed technique is a sequential process. Even though each step is robust, if a poor initial CS reconstruction is performed, it will lead to inexact motion vectors and finally to a low resolution motion corrected image. A comprehensive approach to avoid this kind of limitation may be to merge the three separate steps into a single optimization algorithm (Asif et al., 2012; Odille et al., 2008). On the other hand, the implementation of the proposed technique over a traditional CS framework is computationally more expensive, because three steps must be performed. We used a computer with an Intel(R) Core(TM) i7-3770 CPU @ 3.40 GHz and memory (RAM) capacity of 32.0 GB to run the proposed technique, with the algorithm taking approximately 100 minutes. Speeding up the reconstruction time may be possible by parallel computing techniques.

The proposed method can be extended to 3D CINE liver MRI as an approach for applications where the respiratory signal can be used as a motion surrogate signal, such as is done in coronary MR angiography (Stuber et al., 1999; Spuentrup and Botnar, 2006). In coronary MR angiography, spatial resolution is bounded by breath-hold acquisition (15–20 s) (Spuentrup and Botnar, 2006), but with the emergence of navigator techniques, the spatial resolution is improved by correcting free-breathing acquisitions (Stuber et al., 1999). Using motion corrupted data (avoiding external navigator), a 3D CINE liver MR image may be generated from the motion corrected image obtained in this work. As previously discussed, to reconstruct the motion corrected image  $\hat{\mathbf{m}}_{t_0}$ , we need to solve Equation (10). By employing the acquired data from all the frames  $\mathbf{b}$  and the estimated motion vector operator, the proposed 3D CINE liver is defined as follows:

$$\hat{\mathbf{m}} = \mathbf{V}\hat{\mathbf{m}}_{t_0}. \quad (13)$$

Equation (13) shows how to generate the whole time sequence, where an accurate estimation of the respiratory signal may be obtained through rigid registration in the head-feet (H-F) direction of a region of interest (ROI) including the liver.

## 6 Conclusion

We have presented a recovery algorithm tailored for free-breathing dynamic 3D liver MRI, which demonstrated an increase in imaging efficiency while reducing acquisition time and removing non-rigid motion artifacts. In addition, the recovery algorithm does not sacrifice image quality. In the in-vivo experiments, our framework produced improved signal-to-error ratios with respect to traditional CS technique (with gains up to 6 dB), and accurate complex wavelet structural similarity indexes in comparison with the ground truth. These results demonstrate that it is feasible to achieve high speedups in acquisition time (approximately up to  $R = 10$ ) and remove motion artifacts without diminishing image quality.

## Acknowledgments

The authors acknowledge financial support from CONICYT (Anillo ACT 079), FONDECYT 1100529, and MISTI 2012.

## Appendix

In this section we present the pseudo-code of the proposed we present the pseudo-code of the proposed Motion Corrected Compressed Sensing framework for free-breathing 3D liver MRI. Prior to solve Equation (10), we need to approximate the motion operator  $\mathbf{V}$  using the acquired k-space undersampled data  $\mathbf{b}$ . The pseudo-code is illustrated in Algorithm 1.

---

**Algorithm 1:** Pseudo-code of the computation of motion operator  $\mathbf{V}$ .

---

Initialization;

**for** *each of the  $T$  frames* **do**

Initial reconstruction:  $\hat{\mathbf{m}}_t \leftarrow \left( \arg \min_{\mathbf{m}'} \frac{1}{2} \|\mathbf{S}\mathbf{F}\mathbf{m}' - \mathbf{b}'\|_{\ell_2}^2 + \beta \|\mathbf{m}'\|_{\ell_1} \right)_t + \mathbf{F}^H \bar{\mathbf{b}}$ ;

**end**

Select reference frame  $\hat{\mathbf{m}}_{t_0}$ ;

**for** *each of the  $T$  frames* **do**

Motion vectors estimation:  $\mathbf{V}_t \leftarrow \arg \min_{\mathbf{v}_t} D(\hat{\mathbf{m}}_t, \hat{\mathbf{m}}_{t_0} | \mathbf{v}_t) + w \|\mathbf{k}^T \mathbf{Q} \mathbf{v}_t\|_{\ell_1}$ ;

**end**

**return** *Motion operator  $\mathbf{V}$ .*

---

Using the k-space measurements  $\mathbf{b}$  and the previously computed motion operator  $\mathbf{V}$ , we are able to solve Equation (10) as illustrated in Algorithm 2.

---

**Algorithm 2:** MC-CS recovery.

---

Initialization;

**while** *Stopping criteria not reached* **do**

    Pre-computation of parameters for line-search;

    Line-search for optimal stepsize:

$$t^* \leftarrow \arg \min_t \frac{1}{2} \|\mathbf{SFV}(\mathbf{m}_{t_0} + t\Delta\mathbf{m}_{t_0}) - \mathbf{b}\|_{\ell_2}^2 + \lambda \|\Phi(\mathbf{m}_{t_0} + t\Delta\mathbf{m}_{t_0})\|_{\ell_1};$$

    Motion corrected image update:  $\mathbf{m}_{t_0} \leftarrow \mathbf{m}_{t_0} + t^*\Delta\mathbf{m}_{t_0}$ ;

    Gradient computation:  $g_{new} \leftarrow \mathbf{V}^H \mathbf{F}^H \mathbf{S}^H (\mathbf{SFV}\mathbf{m}_{t_0} - \mathbf{b}) + \lambda \Phi^H |\Phi\mathbf{m}_{t_0}|$ ;

    Search direction:  $b \leftarrow \|g_{new}\|_{\ell_2}^2 / \|g_{old}\|_{\ell_2}^2$ ;

    Gradient update:  $g_{old} \leftarrow g_{new}$ ;

    Conjugate gradient update:  $\Delta\mathbf{m}_{t_0} \leftarrow -g_{new} + b\Delta\mathbf{m}_{t_0}$ ;

**end**

**return**  $\mathbf{m}_{t_0}$ .

---

## References

- S.M. Asif, L. Hamilton, M. Brummer, and J. Romberg. Motion-adaptive spatio-temporal regularization for accelerated dynamic MRI. *Magn. Reson. Med.*, 70(3):800–812, 2012.
- P.G. Batchelor, D. Atkinson, P. Irarrazaval, D. Hill, J. Hajnal, and D. Larkman. Matrix description of general motion correction applied to multi-shot images. *Magn. Reson. Med.*, 54(5):1273–1280, 2005.
- S. Becker, J. Bobin, and E.J. Candes. NESTA: A fast and accurate first-order method for sparse recovery. *SIAM J. Imaging Sciences*, 4(1):1–39, 2011.
- B. Bilgic, V.K. Goyal, and E. Adalsteinsson. Multi-contrast reconstruction with bayesian compressed sensing. *Magn. Reson. Med.*, 66(6):1601–1615, 2011.
- B. Bilgic, K. Setsompop, J. Cohen-Adad, A. Yendiki, L.L. Wald, and E. Adalsteinsson. Accelerated diffusion spectrum imaging with compressed sensing using adaptive dictionaries. *Magn. Reson. Med.*, 68(6):1747–1754, 2012.
- S. Boyd and L. Vandenberghe. *Convex Optimization*. Cambridge University Press, 2004.
- E.J. Candes and T. Tao. Decoding by linear programming. *IEEE Trans. Inform. Theory*, 51(12):4203–4215, 2005.

- E.J. Candes and T. Tao. Near-optimal signal recovery from random projections: Universal encoding strategies? *IEEE Trans. Inform. Theory*, 52(12):5406–5425, 2006.
- E.J. Candes, J. Romberg, and T. Tao. Robust uncertainty principles: exact signal reconstruction from highly incomplete frequency information. *IEEE Trans. Inform. Theory*, 52(2):489–509, 2006a.
- E.J. Candes, J. Romberg, and T. Tao. Stable signal recovery from incomplete and inaccurate measurements. *Commun. Pure Appl. Math.*, 59(8):1207–1223, 2006b.
- H. Chandarana, E. Robinson, C.H. Hajdu, L. Drozhinin, J.S. Babb, and B. Taouli. Microvascular invasion in hepatocellular carcinoma: is it predictable with pretransplant MRI? *AJR Am. J. Roentgenol.*, 196(5):1083–1089, 2011.
- H. Chandarana, T. Block, J. Stepanic, D.K. Sodickson, and R. Otazo. Contrast-enhanced free-breathing perfusion weighted MR imaging of the whole-liver with high spatial and temporal resolution. In *Proc. Intl. Soc. Mag. Reson. Med. 20*, page 4009, Melbourne, Australia, May 2012.
- D. Donoho. Compressed Sensing. *IEEE Trans. Inform. Theory*, 52(4):1289–1306, 2006.
- P.C. Hansen. Analysis of discrete ill-posed problems by means of the L-curve. *SIAM Rev.*, 34(4):561–580, 1992.
- P.C. Hansen. The L-curve and its use in the numerical treatment of inverse problems. In *Computational Inverse Problems in Electrocardiology*, ed. P. Johnston, *Advances in Computational Bioengineering*, pages 119–142. WIT Press, 2000.
- P.C. Hansen and D.P. O’Leary. The use of the L-curve in the regularization of discrete ill-posed problems. *SIAM J. Sci. Comput.*, 14(6):1487–1503, 1993.
- D.L.G. Hill, P.G. Batchelor, M. Holden, and D.J. Hawkes. Medical image registration. *Phys. Med. Biol.*, 46(3):R1–R45, 2001.
- P. Irarrazaval, R. Boubertakh, R. Razavi, and D. Hill. Reconstruction of Undersampled Dynamic Images Based on Time Frame Registration. *Magn. Reson. Med.*, 54(1):1207–1215, 2005.
- H. Jung and J.C. Ye. Motion estimated and compensated compressed sensing dynamic magnetic resonance imaging: what we can learn from video compression techniques. *Int. J. Imaging. Syst. Technol.*, 20(2):81–98, 2010.
- H. Jung, K. Sung, K.S. Nayak, E.Y. Kim, and J.C. Ye. k-t FOCUSS: A general compressed sensing framework for high resolution dynamic MRI. *Magn. Reson. Med.*, 61(1):103–116, 2009.
- J.I. Lee, J.W. Lee, Y.S. Kim, Y.A. Choi, Y.S. Jeon, and S.G. Cho. Analysis of survival in very early hepatocellular carcinoma after resection. *J. Clin. Gastroenterol.*, 45(4):366–371, 2011.

- M. Lustig, D. Donoho, and J.M. Pauly. Sparse MRI: The application of compressed sensing for rapid MR imaging. *Magn. Reson. Med.*, 58(6):1182–1195, 2007.
- M. Lustig, D. Donoho, J. Santos, and J. Pauly. Compressed Sensing MRI. *IEEE Signal Process. Mag.*, 25(2):72–82, 2008.
- S.L. Merlet, M. Paquette, R. Deriche, and M. Descoteaux. Ensemble average propagator reconstruction via compressed sensing: Discrete or continuous bases? In *Proc. Intl. Soc. Mag. Reson. Med. 20*, page 2277, Melbourne, Australia, May 2012.
- A. Myronenko. *Non-rigid Image Registration: Regularization, Algorithms and Applications*. PhD thesis, Department of Science & Engineering School of Medicine, Oregon Health & Science University, Portland, OR, U.S.A., June 2010.
- W.E. Naugler and A. Sonnenberg. Survival and cost-effectiveness analysis of competing strategies in the management of small hepatocellular carcinoma. *Liver Transpl.*, 16(10): 1186–1194, 2010.
- A.Y. Ng. Feature selection, l1 vs. l2 regularization, and rotational invariance. In *Proceedings of the Twenty-first International Conference on Machine Learning (ICML 2004)*, page 78, Banff, Alberta, Canada, July 2004.
- F. Odille, P.A. Vuissoz, P.Y. Marie, and J. Felblinger. Generalized reconstruction by inversion of coupled systems (GRICS) applied to free-breathing MRI. *Magn. Reson. Med.*, 60(1): 146–157, 2008.
- C. Prieto, P.G. Batchelor, D.L. Hill, J.V. Hajnal, M. Guarini, and P. Irarrazaval. Reconstruction of undersampled dynamic images by modeling the motion of object elements. *Magn. Reson. Med.*, 57(5):939–949, 2007.
- M.P. Sampat, Z. Wang, S. Gupta, A.C. Bovik, and M.K. Markey. Complex wavelet structural similarity: a new image similarity index. *IEEE Trans. Image Process.*, 18(11):2385–2401, 2009.
- E. Spuentrup and R.M. Botnar. Coronary magnetic resonance imaging: visualization of the vessel lumen and the vessel wall and molecular imaging of arteriothrombosis. *Eur. Radiol.*, 16(1):1–14, 2006.
- M. Stuber, R.M. Botnar, P.G. Danias, K.V. Kissinger, and W.J. Manning. Submillimeter three-dimensional coronary MR angiography with real-time navigator correction: comparison of navigator locations. *Radiology*, 212(2):579–587, 1999.
- A.N. Tikhonov and V.I. Arsenin. *Solutions of Ill-Posed Problems*. Winston and Sons, 1977.
- M. Usman, D. Atkinson, F. Odille, C. Kolbitsch, G. Vaillant, T. Schaeffter, P.G. Batchelor, and C. Prieto. Motion corrected compressed sensing for free-breathing dynamic cardiac MRI. *Magn. Reson. Med.*, 70(2):504–516, 2012.

- P. Viola and W.M. Wells. Alignment by maximization of mutual information. *Int. J. Comput. Vision*, 24(2):137–154, 1997.
- G. Wright. Magnetic resonance imaging. *IEEE Signal Process. Mag.*, 14(1):56–66, 1997.
- F. Yanez and P. Irarrazaval. Sorted Compressed Sensing in MRI. In *Proc. Intl. Soc. Mag. Reson. Med. 22*, page 1592, Milan, Italy, May 2014.
- F. Yanez, A.P. Fan, B. Bilgic, C. Milovic, E. Adalsteinsson, and P. Irarrazaval. Quantitative Susceptibility Map Reconstruction via Total Generalized Variation Regularization. In *3rd International Workshop on Pattern Recognition in Neuroimaging*, pages 203–206, Philadelphia, PA, USA, June 2013.